We are IntechOpen, the world's leading publisher of Open Access books Built by scientists, for scientists

6,900
Open access books available

186,000
International authors and editors

200M
Downloads

154
Countries delivered to

Our authors are among the

TOP 1%
most cited scientists

12.2%
Contributors from top 500 universities

CLARIVATE ANALYTICS
BOOK CITATION INDEX
INDEXED

WEB OF SCIENCE™

Selection of our books indexed in the Book Citation Index
in Web of Science™ Core Collection (BKCI)

Interested in publishing with us?
Contact book.department@intechopen.com

15

Hybrid Numerical-Experimental Holographic Interferometry for Investigation of Nonlinearities in MEMS Dynamics

Minvydas Ragulskis[1], Arvydas Palevicius[2] and Loreta Saunoriene[3]
[1,3]Research Group for Mathematical and Numerical Analysis of Dynamical Systems,
Kaunas University of Technology, Studentu 50-222, 51638 Kaunas
[2]International Studies Center, Kaunas University of Technology, A. Mickeviciaus 37,
44244 Kaunas
Lithuania

1. Introduction

Holographic interferometry is a powerful experimental technique for analysis of structural vibrations, especially if the amplitudes of those vibrations are in the range of micrometers (Caponero et al. (2000); Fagan et al. (1972); Fein (1997); Ganesan et al. (2000); Rastogi (2000); Vest (1979)). Recent advancements in optical measurement technology and development of hybrid numerical-experimental techniques require application of computational algorithms not only for post-processing applications like interpretation of experimental patterns of fringes, but embedding real time algorithms into the measurement process itself (Ragulskis & Saunoriene (2007)).

Computation and plotting of patterns of time average holographic fringes in virtual numerical environments involves such tasks as modelling of the optical measurement setup, geometrical and physical characteristics of the investigated structure and the dynamic response of the analysed system (Ragulskis et al. (2003)). Calculation of intensity of illumination at any point on the hologram plane requires computation of definite integrals over the exposure time. If the analysed structures perform harmonic oscillations that do not impose any complications – there exist even analytical relationships between the intensity of illumination, amplitude of oscillation, laser wavelength, etc. But if the oscillations of the investigated structures are non-harmonic (what is common when structures are non-linear) and the formation of patterns of fringes is implemented in the real time mode, the calculation of definite integrals becomes rather problematic. One of the objects of this study is to propose an order adaptive algorithm which could be effectively applicable for calculation of definite integrals in different real time holography applications.

Another goal of this study is to show that holographic interferometry, being a non-destructive whole field technique capable of registering micro oscillations of micro electromechanical systems (MEMS) components, cannot be exploited in a straightforward manner (Ostasevicius et al. (2005)). There exist numerous numerical methods and techniques for interpretation of patterns of fringes in the registered holograms of different oscillating objects and surfaces. Unfortunately, sometimes straightforward application of these motion reconstruction

methods (ordinary fringe counting technique, etc.) does not produce acceptable results. A typical example is holographic analysis of a MEMS switch dynamics which will be described in this chapter.

2. Hybrid numerical-experimental optical investigation of non-linearity in MEMS dynamics

2.1 Technological features of the MEMS cantilever

Investigation of dynamics of micro electromechanical systems (MEMS) is an important problem of engineering, technology and metrology. Specifically, recent interest in applying MEMS technology to miniaturization of relays, sensors, actuators for variety of applications requires design of appropriate testing and measurement tools for investigation of dynamic properties of those systems. Though MEMS technology offers great promise in addressing the need for smaller dynamical systems, the development of new types of MEMS structures is very costly and complicated procedure. On the other hand, straight application of principles of design of macro-mechanical systems is rather limited in MEMS applications. Therefore, application of measurement technologies capable of detecting the dynamic properties of micro scale systems may help to understand and evaluate the functionality of the systems.

Hybrid numerical-experimental optical techniques are applied for investigation of micro-mechanical relays, in particular their cantilevers. The apparent simplicity of the problem is misguiding due to non-linear interaction between the cantilever and the bottom electrode. Therefore the results of optical measurements of the cantilever dynamics are inaccurate due to the shift of the fringes in time average laser holographic interferograms. Numerical modelling helps to solve non-uniqueness of the inverse problem and to validate the interpretation of the pattern of fringes.

The fabrication sequence of the micro-electromechanical switch begins with the patterning and reactive ion etching of silicon using SF_6/N_2 gas chemistry in the cantilever source (support) area fabricating microstructures to increase the cantilever bond strength either durability of the device. After treatment of the substrate in the O_2/N_2 gases mixture plasma chrome layer of about 30 nm thickness and gold layer of about 200 nm thickness were deposited. Patterning of the source, gate and drain electrodes were performed using lift-off lithography. Electron beam evaporation was performed to deposit a sacrificial copper layer with thickness of about 3000 nm. Copper layer covered the whole area of the substrate. Patterning of the copper layer was performed in two steps. First of all, the copper layer was partially etched (etchant: H_2SO_4:CrO_3:H_2O) to define the contact tips for the cantilever and etching duration directly determined the spacing between tip's top and drain electrode. Next, the copper layer was etched away to uncover the source cantilever support area. The next step was photo resist patterning on the top of the sacrificial layer to define the mask for the cantilever sector and lift-off lithography of the evaporated gold layer with thickness of about 200 nm was performed. Afterwards, the photoresist was spun and patterned once again in the same sector and thick nickel layer was electroplated (sulfamate electrolyte: $Ni(NH_2SO_3)_2$:$4H_2O$) fabricating cantilever structure. Finally, the sacrificial layer was removed away using the same wet copper etchant to release the free-standing cantilever. The general view of MEMS cantilever is presented in Fig.1.

Figure 2 presents time average holograms of the previously described cantilever. The method used for registering optical holograms is described in Ostasevicius et al. (2004). Figure 2 (a) presents a hologram of acoustically excited cantilever. Figure 2(b) presents a hologram of cantilever excited by oscillating charge of the drain electrode.
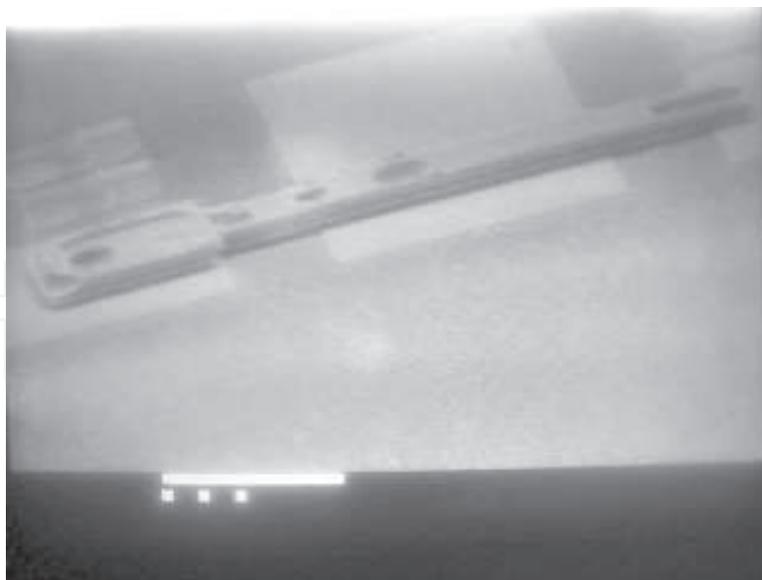
Fig. 1. Microscopic photo of MEMS cantilever

(a)   (b)
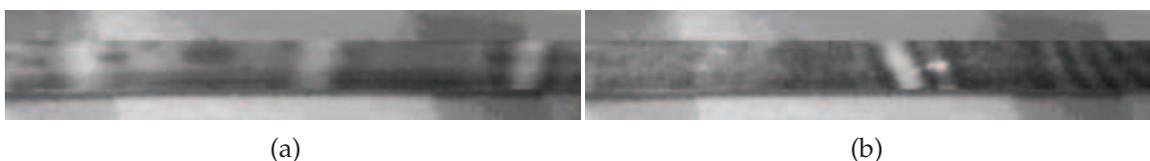
Fig. 2. Holograms of cantilever: (a) acoustically excited cantilever; (b) excited by oscillating charge

Interpretation of hologram in Fig. 2(a) is straightforward – white fringes are regularly distributed on the surface of cantilever and ordinary fringe counting techniques can be applied for the reconstruction of the field of vibration amplitudes. The interpretation of pattern of fringes in Fig. 2(b) is much more complicated – one white and several dark fringes are distributed on the surface of cantilever and it is quite difficult to understand the dynamics of the cantilever. Moreover, longer exposure times produce dark images when the cantilever is excited by oscillating charge and the pattern of fringes is sensitive to exposure time. Such effects probably are caused by specific dynamical properties of the system.

Difficulties in interpretation of the generated patterns of fringes in holograms of MEMS cantilevers excited by oscillating charge originated the necessity for developing hybrid numerical-experimental models of analysed systems. Simulation of the dynamic as well as optical processes taking place in the analysed systems could help understanding experimental results.

2.2 Phenomenological model of MEMS cantilever

First step in analysing complex MEMS cantilever system is developing of simple one-dimensional phenomenological model which is presented in Fig. 3.

Governing equation of motion of the system presented in Fig. 3 takes the following form:

$$m\ddot{x} + h\dot{x} + kx = F_e(x),$$ (1)

where m, h, k – mass, viscous damping and stiffness coefficients; x – coordinate; F_e – electrostatic force; top dots denote full derivatives by time t. It is assumed that the charged
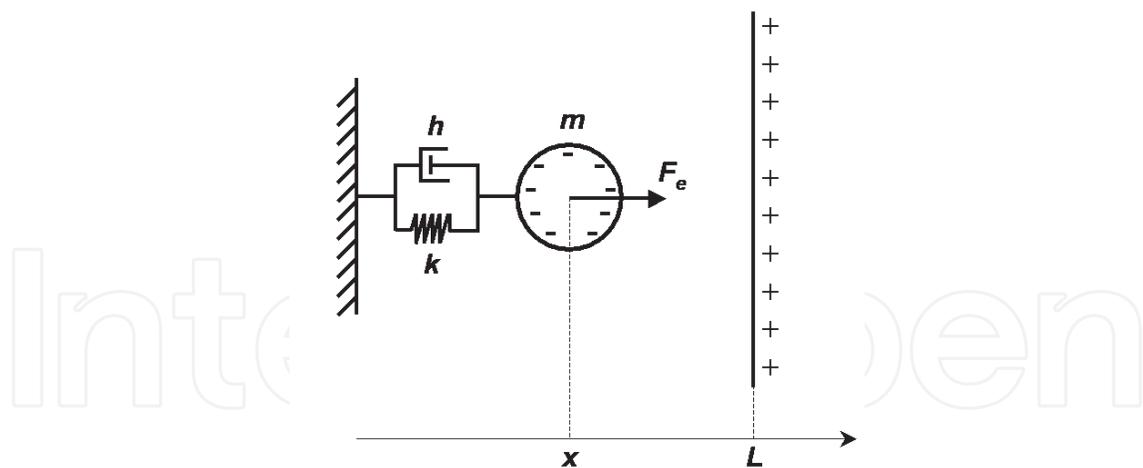
Fig. 3. One degree of freedom model of MEMS cantilever

contact plane is motionlessly fixed at coordinate L (Fig. 3). Mass m is negatively charged, while the charge Q of the contact plane varies harmonically in time:

$$Q = q \sin(\omega t), \tag{2}$$

where q – maximum charge of the contact plane; ω – frequency of charge oscillation. Then the electrostatic force F_e acting to mass m is

$$F_e = C \frac{Q}{L - x}, \tag{3}$$

where constant C depends from the charge of mass m, density of air, etc.

Harmonic oscillation of the charge of the contact plane can excite strongly non-linear response. That is a natural result as the governing equation of motion is non-linear. The non-linearity of the motion of the mass m is especially clear when the frequency of charge oscillation is around the natural frequency of the mechanical system (Fig. 4). In practical applications the frequency of charge oscillation very rarely reaches the fundamental frequency of the MEMS cantilever only due to the fact that it is very high. Usually the excitation frequencies are of magnitude lower than fundamental frequencies.

The presented one degree of freedom cantilever model is analysed when the excitation frequency is much lower that the fundamental frequency. It can be noted that the differential equation turns to be stiff and special care is required applying direct time marching integration techniques. First the system is integrated until the transient processes cease down. Then the attractor in phase plane $x - \dot{x}$ is drawn. Repetition of such procedure at different values of maximum charge q produces an array of attractors as shown in Fig. 5. It can be noted that the motion of the mass m is almost linear at small excitation. The form of the stable attractor gradually deforms at increasing excitation what is a natural result for a non-linear system.

One of the classical techniques used for experimental analysis of MEMS cantilevers is time average laser holography. It is a non-destructive whole field technique capable of detection microscopic dynamic displacements of the objects performing harmonic vibrations. How could the experimental results be interpreted if the analysed object would oscillate not harmonically, but as shown in Fig. 5.

One-dimensional system is considered for simplicity. Then the intensity of illumination I in the hologram plane will be:
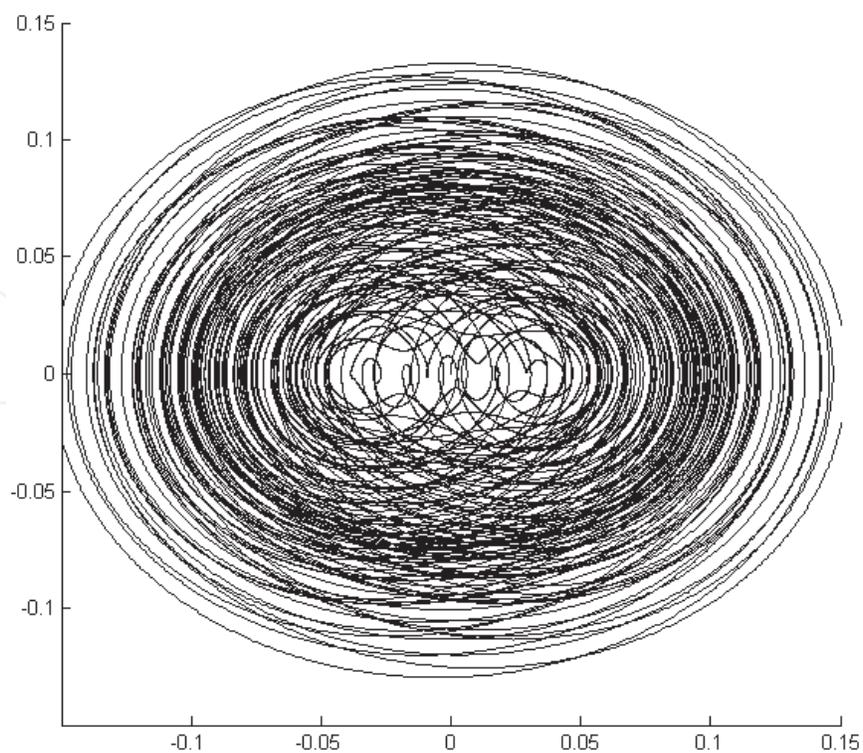
Fig. 4. Chaotic motion of mass m in phase plane $x - \dot{x}$ at $m = 1$; $k = 1$; $h = 0.003$; $\omega = 0.73$; $q = 0.1$; $L = 2$
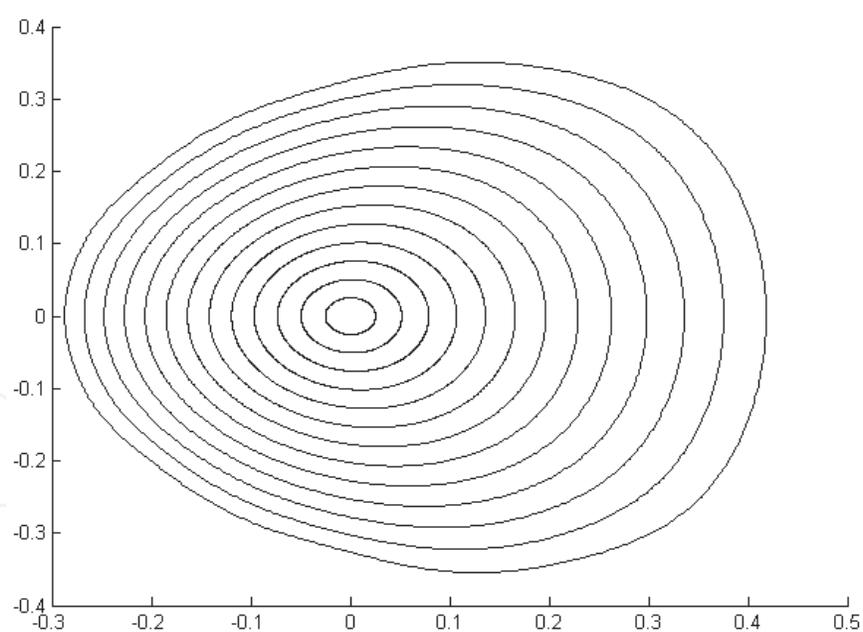
Fig. 5. Stable attractors at $m = 0.25$; $k = 20$; $h = 0.1$; $\omega = 1$; $L = 2$; $q = 1, 2, \ldots 13$

$$I = \lim_{T \to \infty} \frac{1}{T^2} \left| \int_0^T \exp\left(j \frac{2\pi}{\lambda} \zeta(t) \right) dt \right|^2, \qquad (4)$$

where T – exposure time; λ – laser wavelength; ζ – scalar time process; j – imaginary unit. When $\zeta(t) = u\sin(\omega t + \varphi)$ where u, ω, φ – amplitude, angular frequency and phase of oscillations, the intensity of illumination takes the form:

$$I = \left| J_0\left(\frac{2\pi}{\lambda}u\right) \right|^2 = \lim_{T\to\infty}\frac{1}{T^2}\left(\int_0^T \cos\left(\frac{2\pi}{\lambda}u\sin(\omega t + \varphi)\right)dt \right)^2$$

$$\approx \left(\frac{1}{m}\sum_{i=1}^{m}\cos\left(\frac{2\pi}{\lambda}u\sin\left(\frac{2\pi}{m}(i-1)\right)\right) \right)^2, \tag{5}$$

where J_0 – zero order Bessel function of the first kind. It can be noted that $\lim_{T\to\infty}\int_0^T \sin\left(\frac{2\pi}{\lambda}u\sin(\omega t + \varphi)\right)dt = 0$ due to evenness of the sine function, and that the angular frequency and phase have no effect to the intensity of illumination. The second approximate equality builds the ground for numerical modelling of the relationships governing the formation of interference fringes.

If $\zeta(t)$ is not a harmonic process the intensity of illumination can be numerically reconstructed from Eq. (4), but the calculation is more complex than in Eq. (5) due to the fact the integral $\lim_{T\to\infty}\int_0^T \sin\left(\frac{2\pi}{\lambda}\zeta(t)\right)dt$ does not converge to zero. If $\zeta(t)$ is a periodic process and T_p is the time length of the period, the approximate numerical calculation scheme takes the following form:

$$I \approx \left(\frac{1}{m}\sum_{i=1}^{m}\cos\left(\frac{2\pi}{\lambda}\zeta\left(t_0 + \frac{T_p}{m}(i-1)\right)\right) \right)^2 + \left(\frac{1}{m}\sum_{i=1}^{m}\sin\left(\frac{2\pi}{\lambda}\zeta\left(t_0 + \frac{T_p}{m}(i-1)\right)\right) \right)^2, \tag{6}$$

where t_0 – arbitrary selected time moment. If $\zeta(t)$ is a process characterising time history of a dynamical system setting to a stable limit cycle type attractor, time moment t_0 must be selected large enough so that the transient processed are ceased. Such calculations are performed for an array of attractors shown in Fig. 6. One hundred separate solutions of Eq. (1) are analysed at intermittent values of q in the range from 0 to 13. The produced intensities of illumination are presented in Fig. 6 (x axis denotes 100 separate problems).

Remarkable is the fact that the relationship between the intensity of illumination and parameter q holds the same character as the square of Bessel function in Eq. (5). In other words, the inverse problem of the reconstruction of dynamic displacements does not have a unique solution. Interference fringes can be formed when the analysed object performs harmonic vibrations. Very similar interference fringes will be formed when the object will perform non-linear periodic oscillations. Thus though time average laser holography is a very attractive technique for analysis of MEMS cantilever vibrations, the interpretation of experimentally produced interference fringes is rather complex procedure if one cannot be sure if the vibrations are harmonic. This effect is illustrated in Fig. 7. The presented non-linear periodic oscillation and harmonic vibration will both generate the same intensity of illumination corresponding to the centre of the sixth interference fringe. It can be noted that time average laser holography is insensitive to static shifts of harmonic oscillations. That follows from the property of Bessel function:
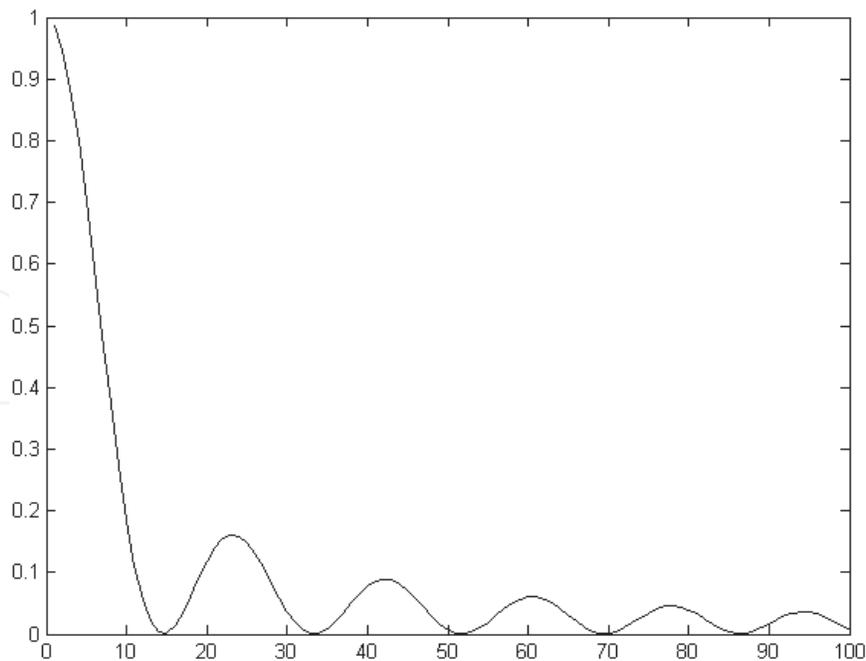
Fig. 6. Relationship between intensities of illumination and parameter q

$$\lim_{T \to \infty} \frac{1}{T^2} \left| \int_0^T \exp\left(j\frac{2\pi}{\lambda} \left(u \sin(\omega t + \varphi) + C \right) \right) dt \right|^2$$

$$= \lim_{T \to \infty} \frac{1}{T^2} \left| \int_0^T \exp\left(j\frac{2\pi}{\lambda} \left(u \sin(\omega t + \varphi) \right) \right) dt \right|^2 = \left(J_0 \left(\frac{2\pi}{\lambda} u \right) \right), \tag{7}$$

where C – constant. Results presented in Fig. 7 are remarkable not for the difference between the averages of non-linear and harmonic vibrations. Interesting is the fact that two different trajectories generate same intensity of illumination.

The problem of reconstruction of dynamic displacements from a pattern of interference fringes is even more complicated when the oscillations are chaotic. In that case the illumination of intensity can be calculated for certain stochastic time series approximating process $\zeta(t)$. If a time series ζ_i is normally distributed with variance σ^2 then, the decay of intensity of illumination can be calculated as follows:

$$I \approx \lim_{m \to \infty} \left(\left(\frac{1}{m} \sum_{i=1}^{m} \cos\left(\frac{2\pi}{\lambda} \zeta_i \right) \right)^2 + \left(\frac{1}{m} \sum_{i=1}^{m} \sin\left(\frac{2\pi}{\lambda} \zeta_i \right) \right)^2 \right)$$

$$= \lim_{m \to \infty} \left(\frac{1}{m} \sum_{i=1}^{m} \sum_{k=0}^{+\infty} \frac{(-1)^k \left(\frac{2\pi}{\lambda} \zeta_i \right)^{2k}}{(2k)!} \right)^2 = \left(\sum_{k=0}^{+\infty} \frac{(-1)^k \left(\frac{2\pi}{\lambda} \right)^{2k}}{(2k)!} \lim_{m \to \infty} \sum_{i=1}^{m} \frac{(\zeta_i)^{2k}}{m} \right)^2$$

$$= \left(\sum_{k=0}^{+\infty} \frac{(-1)^k \left(\frac{2\pi}{\lambda} \right)^{2k}}{(2k)!} \cdot (2k-1)!! \cdot \sigma^{2k} \right)^2 = \left(\sum_{k=0}^{+\infty} \frac{(-1)^k \left(\frac{2\pi}{\lambda} \sigma \right)^{2k}}{(2k)!!} \right)^2 \tag{8}$$

$$= \left(\sum_{k=0}^{+\infty} \frac{(-1)^k \left(\frac{2\pi}{\lambda} \sigma \right)^{2k}}{2^k k!} \right)^2 = \left(\sum_{k=0}^{+\infty} \frac{(-1)^k}{k!} \left(\frac{1}{2} \left(\frac{2\pi}{\lambda} \sigma \right)^2 \right)^k \right)^2 = \exp^2 \left(-\frac{1}{2} \left(\frac{2\pi}{\lambda} \sigma \right)^2 \right).$$

The following identities are used in Eq. (8). If $\zeta \sim N(0, \sigma^2)$, then
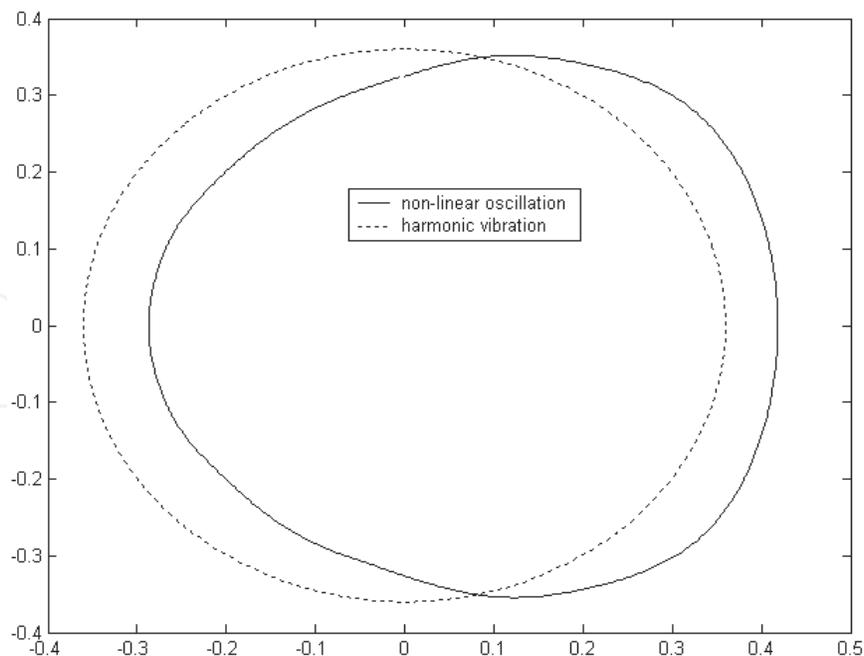
Fig. 7. Two different trajectories generating same intensity of illumination

$$
E\zeta^{2k-1} \equiv 0, \quad k = 1, 2, 3, \ldots;
$$
$$
E\zeta^{2k} \equiv 1 \cdot 3 \cdot \ldots \cdot (2k-1)\, \sigma^{2k} = (2k-1)!!\sigma^{2k}, \quad k = 1, 2, 3, \ldots.
\tag{9}
$$

It can be noted, that in this case no interference fringes will be formed at all – the intensity of illumination will gradually decrease at increasing variance σ^2.

This is a classical example of an ill-posed inverse problem. The problem of reconstruction of motion from a pattern of interference fringes has a unique solution only if the vibration of the analysed structure is harmonic. When the oscillations are non-linear (what is likely in MEMS cantilever dynamics) the interpretation of pattern of fringes can be complicated. Next sections address questions related to numerical construction of time averaged holographic interferograms and computational aspects of the calculation of definite integrals in real time applications.

3. Order adaptive quadrature rule for real time holography applications

As mentioned previously, computation of the intensity of illumination at any point on the hologram plane requires computation of definite integrals over the exposure time. But standard higher order Newton-Cotes quadrature formulas (Davis & Rabinowitz (1984)) require that the number of nodes must be a divisible numeral. For example the second order Newton-Cotes rule already requires that the number of nodes must be odd. Such conditions mean that a significant number of nodes at the end of an experimental time series must be deleted and the integration interval artificially shortened for higher order Newton-Cotes rule, if the number of nodes is not known at the beginning of the experiment. Therefore there exists a definite need for a high order integration rule with a constant time step without any requirement for the number of time steps. Such quadrature formula is proposed in Ragulskis & Saunoriene (2008):

$$\int_{t_0}^{t_0+(k-1)h} f(t)\, dt = \left(\sum_{i=1}^{m} a_i f_i + \sum_{i=1}^{k-2m} f_{m+i} + \sum_{i=1}^{m} a_{m-i+1} f_{k-m+i} \right) h, \tag{10}$$

where a_i are the weights and f_i are the discrete values of sampled function f at time moments $t_0 + (i-1) \cdot h$, $i = 1, \ldots, k$. It has been proved that this integration rule is exact when the integrated function is a polynomial of the m-th order, if only m is odd (Ragulskis & Saunoriene (2008)). The numerical values of the weights a_i are presented in the Table 1 at different values of m. The parameter p in this table denotes the maximum order of exactly integrated polynomials; l is the order of the error term expressed in the form $O(h^l)$.

m	2	3	4	5	6	7
a_1	0.5	0.37500000	0.33333333	0.32986111	0.31875000	0.30422454
a_2	1	1.1666667	1.2916667	1.3208333	1.3763889	1.4603836
a_3		0.95833333	0.83333333	0.76666667	0.65555556	0.45346396
a_4			1.0416667	1.1013889	1.2125000	1.4714286
a_5				0.98125000	0.92569444	0.73939319
a_6					1.0111111	1.0824735
a_7						0.98863261
p	1	3	3	5	5	7
l	2	4	4	6	6	8

Table 1. Nodal weights of the integration rule

It can be noted that finite element method was used for the derivation of the proposed quadrature rule which can be interpreted as a new variant of Gregory type formulas (Davis & Rabinowitz (1984)). Unfortunately, the proposed quadrature rule (also Gregory type rules) can be used only when the order is predefined before the experiment and does not change over the integration process. This paper proposes a multi-processor parallel algorithm with full order adaptability in real time calculation mode.

3.1 The basic real time integration rule
Let's suppose that function f is sampled starting from t_0 at equally spaced time steps; the length of a time step is h. Due to the real time process the number of nodes is not predefined before the experiment and process continues until the end of the sampling. Let's suppose that the terminal moment of the sampling occurs at $t_0 + 7h$ (8 function values f_i, $i = 1, \ldots, 8$ are produced during the sampling process). Order of the integration rule is predetermined to be $m = 3$.

1. The first sum on the right side of Eq. (10) is computed:

$$Sum_1 = a_1 f_1 + a_2 f_2 + a_3 f_3, \tag{11}$$

   where $a_1 = 0.375$, $a_2 = 1.1666667$, $a_3 = 0.95833333$ (Table 1).

2. Starting from the fourth node, the following sum is computed until the end of the time series:

$$Sum_2 = f_4 + f_5 + f_6 + f_7 + f_8. \tag{12}$$

3. When the sampling is terminated, reverse computation of the third sum of eq. (10) is done:

$$Sum_3 = (a_3 - 1) f_6 + (a_2 - 1) f_7 + (a_1 - 1) f_8. \tag{13}$$

4. Finally, the definite integral $\int_{t_0}^{t_0+7h} f(t)\, dt$ is calculated according to eq. (10):

$$I = (Sum_1 + Sum_2 + Sum_3)\, h. \tag{14}$$

The process can terminate at any time step, if only $k \geq 2m$, but the last three values of the sampled function must be saved at every time moment in order to calculate Sum_3.

Now we will generalize the presented example for m-th order integration rule, if only the minimum number of nodes is $2m$. The algorithm is based on Master-Worker paradigm (Mattson et al. (2004)). Schematic graphical representation in Fig. 8 helps to interpret the computation process.
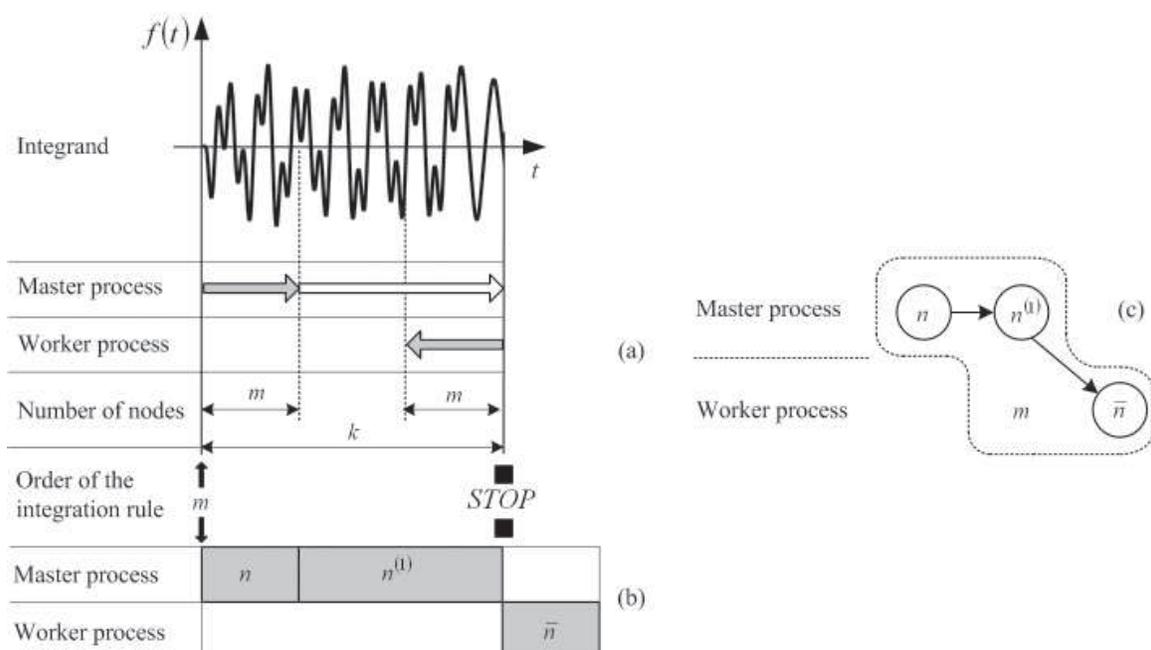

Fig. 8. Schematic representation of the basic model:(a) signal diagram; (b) time diagram; (c) flow chart diagram

Several notations used in Fig. 8 can be explained in more detail. Order of the integration rule m is predefined before the experiment. Calculation of Sum_1 is performed by Master processor (grey right arrow in signal diagram; block n in time diagram and node n in flow chart diagram). After m terms are included into Sum_1, the Master processor continues summation of nodal values of the integrand until the sampling process is terminated (white right arrow in signal diagram; block $n^{(1)}$ in time diagram and node $n^{(1)}$ in flow chart diagram). When the sampling is over, Worker processor performs reverse calculation of Sum_3 (grey left arrow in signal diagram; block $\bar{n}$ in time diagram and node $\bar{n}$ in flow chart diagram).

It can be noted that the last m values of the sampled function must be remembered at every time node in order to calculate Sum_3.

3.2 Order adaptive algorithm for real time applications

The presented basic real time integration rule copes well with integrands which can be approximated by a polynomial of a definite order in the domain of integration. But if the variation of the integrand is fast in some regions and slow in another regions, then order adaptability should be used to increase the accuracy of a definite integral. One can suggest to select very large m at the beginning of the experiment, but then we may face the risk that $k < 2m$.

We assume that there exists a detector which measures the values of the integrand and recommends the order of integration rule at any time moment in the domain of integration. Let's assume that the present order is m_1 and the detector recommends order m_2. Then two different situations may occur. If the number of sampled nodes since m_1 was declared is higher than or equal to $2m_1$, the transition to order m_2 can be performed fluently. The Master processor starts calculating Sum_1 for order m_2, while Worker processor takes care for reverse calculation of Sum_3 for terminated m_1.

But if the number of sampled nodes since m_1 was declared is less than $2m_1$, the Worker processor cannot start reverse calculation of Sum_3 without damaging Sum_1. Therefore a much more complex transition to order m_2 takes place in this situation. If m_2 is higher than m_1 the Worker processor must return to the point where order m_1 was declared and must recalculate Sum_1 with order m_2. But the simplicity is misleading – the Master processor has already summated Sum_1 with order m_1 to the total sum! Therefore the Worker processor must evaluate different weighting coefficients for orders m_1 and m_2. Moreover, the length of the queue where the last function values are stored must be already not m_i, but $2m_i$ (here m_i is the current order).

If m_2 is lower than m_1, but the number of sampled nodes since m_1 was declared is less than $2m_1$, the integration with order m_1 must be continued until the number of nodes is equal to $2m_1$, and only after that the order m_2 can be accepted.

Finally, we may comment what would happen if the sampling process is terminated and the number of sampled nodes since m_i was declared is lower than $2m_i$. Unfortunately, there will be no any possible techniques to preserve order m_i (time step is constant and reverse sampling with smaller time step is impossible in real time mode). The only solution is to select maximum possible order for the available number of time steps (floored half of the number of time steps). We will illustrate the described situations with the following example (Fig. 9 and Fig. 10).

One Master processor and two Worker processors are necessary for full real time mode. Algorithm control, integrand sampling and summation of sums Sum_1 and Sum_2 is performed by Master processor. The Worker processors run only when the order is changed. Worker processors send back the results to the Master processor.

As an extreme situation we describe the transition from order m_3 to order m_4 (Fig. 9) where the second Worker processor is necessary for real time integration. Master processor starts calculating Sum_1 (with weights corresponding to order m_3) as soon as the order m_3 is declared. The number of discrete time nodes necessary for this procedure is m_3. As soon as Sum_1 is finished, Master processor starts summing non-weighted discrete function values. This process continues until order m_4 is declared. But the order detector has sensed a burst in the digital time series, so m_4 is much higher than m_3. In this particular situation we have that m_4 is even greater than k_3 (Fig. 9). Thus, the Worker processor must recalculate both the old Sum_1 and the rest non-weighted part (n_3 and $n_3^{(1)}$ in time diagram). Moreover, at the same time Sum_3 for order m_2 must be accomplished ($\bar{n}_2$ in time diagram). Thus Worker-2 processor is unavoidable for real time computation ($\bar{n}_2$ and $\bar{n}_3$ overlap in time diagram).
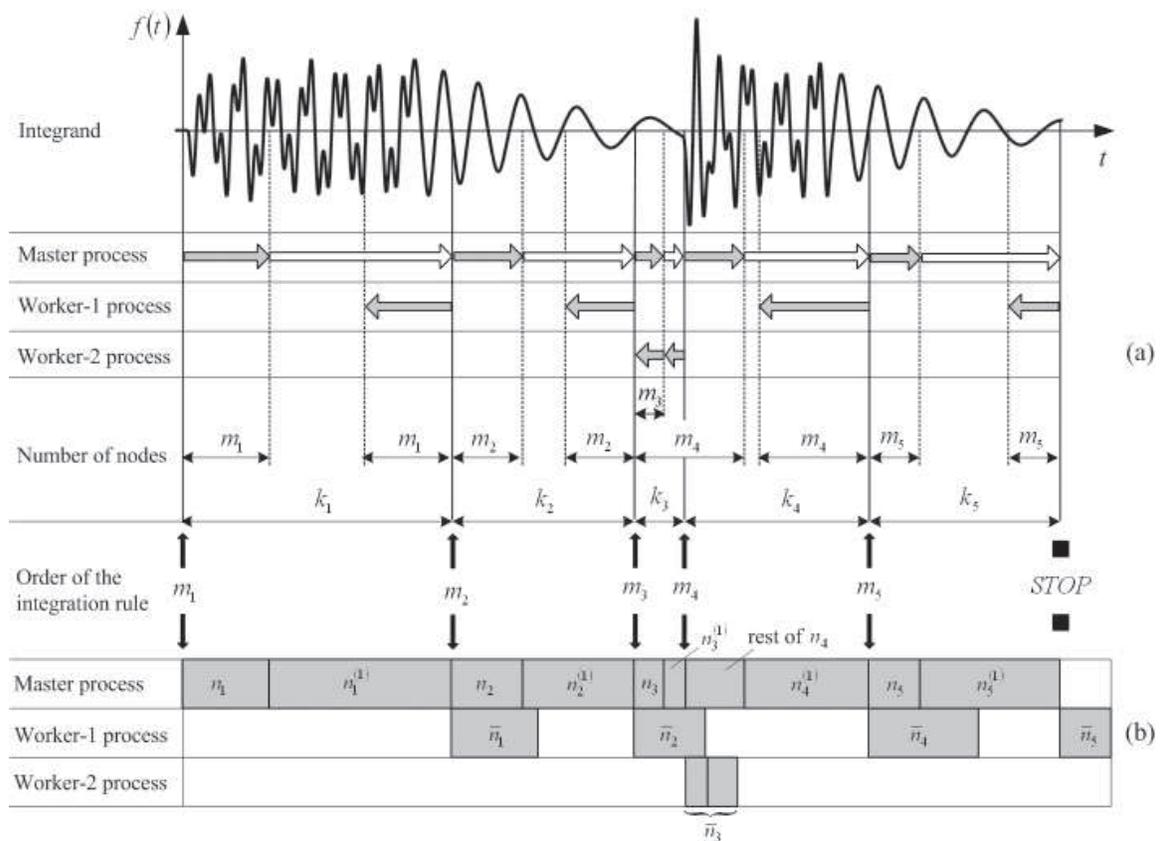
Fig. 9. Real time integration, general case: (a) signal diagram; (b) time diagram
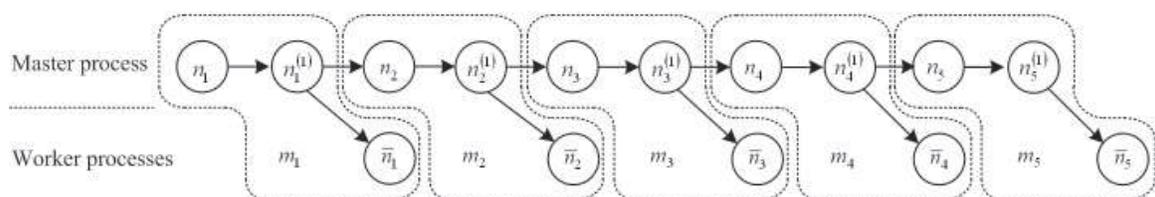
Fig. 10. Real time integration, general case: flow chart diagram

The presented procedure for real time calculation of definite integrals can be effectively applied in hybrid numerical-experimental techniques where time average intensities of illumination are reconstructed in virtual computational environment. Implementation of the proposed integration rule enables full real time computations with minimal data queue lengths and effective management of integration order.

4. Plotting holographic interferograms for visualisation of dynamic results from finite element calculations

The amount of data produced by finite element calculation places a particular challenge to scientific visualization. Meaningful and accurate visualization is an important task of computer modeling, especially when hybrid numerical-experimental techniques are used to construct digital holographic interferograms of such objects as non-linear MEMS cantilevers. Procedures plotting computer generated interferograms from the results of FEM analysis based on the principles of optical holography can provide realistic view of dynamic processes

taking place in such structures. Detailed description of the formation of digital holographic interferograms applicable for hybrid numerical-experimental techniques will be given in this chapter.

4.1 The coupling of FEM model with optical relationships

Let the planes A and B be defined in the 3 dimensional space (Fig. 11). Let the triangle defined by points 1, 2 and 3 be located in the plane A. This triangle is interpreted as an elementary body surface unit meshed using the Finite Element Method. Let the coordinates of the point r_1 define the observation point and the projection plane be defined by the points r_2, r_3 and r_4:

$$r_i = (x_i, y_i, z_i), \quad i = 1, 2, 3, 4, \tag{15}$$

where r_2 is the origin of the projection plane and the vectors $(r_3 - r_2)$, $(r_4 - r_2)$ form the ortho-normal base of the projection plane. The L – coordinates of the point of intersection of the line defined by the point of the structure (x, y, z) and the observation point with the projection plane can be obtained using the relationship in Appendix A, where the system matrix is substituted by:

$$\begin{bmatrix} x_2 & x_3 & x_4 & -x_1 & -x \\ y_2 & y_3 & y_4 & -y_1 & -y \\ z_2 & z_3 & z_4 & -z_1 & -z \\ 1 & 1 & 1 & 0 & 0 \\ 0 & 0 & 0 & 1 & 1 \end{bmatrix}. \tag{16}$$
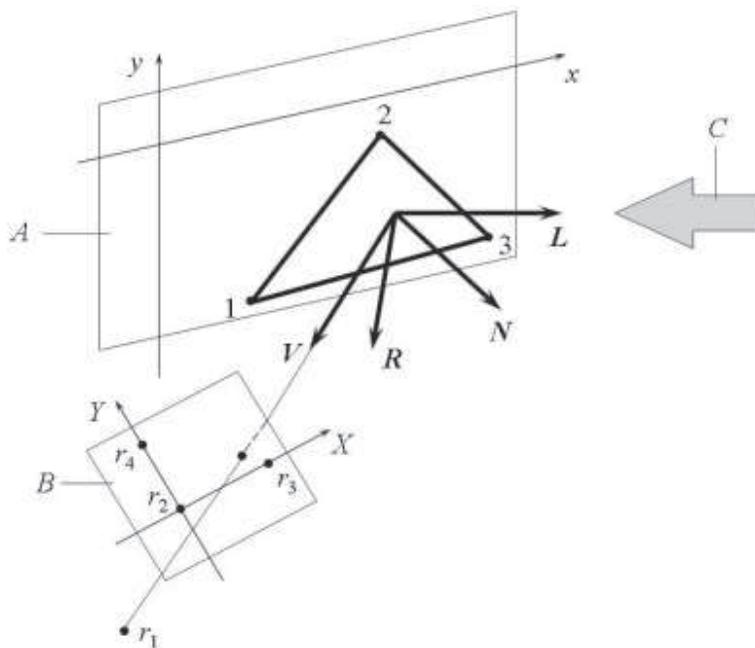

Fig. 11. Determination of the intensity of the surface: A – plane of the structure, B – projection plane, C – the incident laser beam

Then the spatial coordinates of the point of intersection $(\tilde{x}, \tilde{y}, \tilde{z})$ are:

$$\begin{aligned} \tilde{x} &= L_4 x_1 + L_5 x, \\ \tilde{y} &= L_4 y_1 + L_5 y, \\ \tilde{z} &= L_4 z_1 + L_5 z. \end{aligned} \tag{17}$$

The coordinates of the point (X, Y) in the projection plane can be obtained:

$$X = (\tilde{x} - x_2)(x_3 - x_2) + (\tilde{y} - y_2)(y_3 - y_2) + (\tilde{z} - z_2)(z_3 - z_2),$$
$$Y = (\tilde{x} - x_2)(x_4 - x_2) + (\tilde{y} - y_2)(y_4 - y_2) + (\tilde{z} - z_2)(z_4 - z_2). \tag{18}$$

Assuming the projection plane corresponds to the computer graphical screen and contains n rows and m columns of pixels, the calculations are performed for every pixel of the mapped interferogram:

$$X = X_{\min} + (j - 1)(X_{\max} - X_{\min})/(m - 1),$$
$$Y = Y_{\max} - (i - 1)(Y_{\max} - Y_{\min})/(n - 1), \tag{19}$$
$$i = 1, ..., n; \quad j = 1, ..., m,$$

where the subscripts min and max indicate the minimum and maximum values of the corresponding quantities.

The unit normal vector of the projection plane is:

$$x_0 = (y_3 - y_2)(z_4 - z_2) - (z_3 - z_2)(y_4 - y_2),$$
$$y_0 = (z_3 - z_2)(x_4 - x_2) - (x_3 - x_2)(z_4 - z_2), \tag{20}$$
$$z_0 = (x_3 - x_2)(y_4 - y_2) - (y_3 - y_2)(x_4 - x_2).$$

Finally the spatial coordinates (x^*, y^*, z^*) of the point in the projection plane can be determined from:

$$\begin{bmatrix} x_3 - x_2 & y_3 - y_2 & z_3 - z_2 \\ x_4 - x_2 & y_4 - y_2 & z_4 - z_2 \\ x_0 & y_0 & z_0 \end{bmatrix} \begin{Bmatrix} x^* \\ y^* \\ z^* \end{Bmatrix}$$
$$= \begin{Bmatrix} X + x_2(x_3 - x_2) + y_2(y_3 - y_2) + z_2(z_3 - z_2) \\ Y + x_2(x_4 - x_2) + y_2(y_4 - y_2) + z_2(z_4 - z_2) \\ x_2 x_0 + y_2 y_0 + z_2 z_0 \end{Bmatrix}. \tag{21}$$

It is assumed that the analysed structure is located in the plane $z = 0$ in the status of equilibrium, and $(\hat{x}_i, \hat{y}_i)$, $i = 1, 2, 3$ are nodal coordinates of a linear triangle element. Then the L-coordinates can be determined using the relationship in Appendix A, where the system matrix is substituted by:

$$\begin{bmatrix} \hat{x}_1 & \hat{x}_2 & \hat{x}_3 & -x_1 & -x^* \\ \hat{y}_1 & \hat{y}_2 & \hat{y}_3 & -y_1 & -y^* \\ 0 & 0 & 0 & -z_1 & -z^* \\ 1 & 1 & 1 & 0 & 0 \\ 0 & 0 & 0 & 1 & 1 \end{bmatrix}. \tag{22}$$

Thus the approximate coordinates of the intersection point $(\alpha, \beta, 0)$ between the line through the observation point and the pixel (i, j) and the surface of the analysed structure are obtained by interpolation.

It is assumed that the laser rays are coherent and parallel to each other.

The unit vector L from the point of the structure in the state of equilibrium to the isophase cross section of the laser beam in the direction of the beam is predefined.

The normal vector N coincides with the unit vector of the z axis:

$$N = [N_x, N_y, N_z]^T = [0, 0, 1]^T, \tag{23}$$

The relationship between the direction to the light source and the direction of reflection can be described by the following equation (Ivanov & Batrakov (1995)):

$$R = \begin{bmatrix} 2N_x^2 - 1 & 2N_xN_y & 2N_xN_z \\ 2N_xN_y & 2N_y^2 - 1 & 2N_yN_z \\ 2N_xN_z & 2N_yN_z & 2N_z^2 - 1 \end{bmatrix} \cdot L, \tag{24}$$

where R is the direction of reflection. The vectors L, N, R (Fig. 11) are complanar, the angle between L and N is equal to the angle between N and R.

Higher order elements can be subdivided into triangles and the approximate local coordinates of the element can be obtained by interpolation from the local coordinates of the nodes of the triangle.

For the three dimensional problem the calculations are performed for a sequential number of values of the local coordinates (ξ, η) in the current finite element:

$$\begin{aligned} \xi &= -1 + \tfrac{2}{n-1}(i-1), \quad i = 1, ..., n, \\ \eta &= -1 + \tfrac{2}{n-1}(j-1), \quad j = 1, ..., n. \end{aligned} \tag{25}$$

The spatial orthogonal Cartesian coordinates of these points can be calculated using the shape functions of the analysed finite element. Afterwards the corresponding values X and Y are obtained from Eq. (18).

The reconstructed digital image consists of the matrix of pixels where the columns are indexed from 0 to m_x and the rows – from 0 to m_y. Thus the point (X, Y) is mapped to the pixel (i_x, i_y):

$$\begin{aligned} i_x &= \text{round}\left(\tfrac{X - X_{\min}}{X_{\max} - X_{\min}} m_x\right), \\ i_y &= \text{round}\left(m_y - \tfrac{Y - Y_{\min}}{Y_{\max} - Y_{\min}} m_y\right). \end{aligned} \tag{26}$$

The rounding operation in Eq. (26) can distort the quality of the reconstructed image, especially when the resolution of the digital image is low, or the density of interference bands is high. Therefore, the shift operation to the coordinates of the center of the corresponding pixel (i_x, i_y) is introduced:

$$\begin{aligned} X &= i_x \tfrac{X_{\max} - X_{\min}}{m_x} + X_{\min}, \\ Y &= Y_{\min} - (i_y - m_y) \tfrac{Y_{\max} - Y_{\min}}{m_y}. \end{aligned} \tag{27}$$

Now, the spatial coordinates of the center of the pixel (x^*, y^*, z^*) can be calculated from Eq. (21). As the projection of the analysed point on the surface of the structure does not necessary coincide with the center of the pixel, the further calculations are dedicated for the location of a point on the surface corresponding to the center of that pixel.

The tangential vectors to the surface of the analysed finite element

$$\begin{bmatrix} x_\xi & y_\xi & z_\xi \\ x_\eta & y_\eta & z_\eta \end{bmatrix} \tag{28}$$

are determined by multiplying the derivatives of the shape functions (with respect to the local coordinates) by the nodal coordinates of the corresponding finite element. Subscripts in Eq. (28) denote partial derivatives.

The L–coordinates of intersection of the line (guided through the observation point and the center of the pixel) with the plane tangential to the analysed finite element are obtained from the relationship in Appendix A, where the system matrix is substituted by:

$$\begin{bmatrix} x & x + x_\xi & x + x_\eta & -x_1 & -x^* \\ y & y + y_\xi & y + y_\eta & -y_1 & -y^* \\ z & z + z_\xi & z + z_\eta & -z_1 & -z^* \\ 1 & 1 & 1 & 0 & 0 \\ 0 & 0 & 0 & 1 & 1 \end{bmatrix}. \tag{29}$$

Thus the calculations are performed for the corrected local coordinates $(\xi + L_2, \eta + L_3)$. It can be noted that such modifications make the procedure more precise and lowers the noise effects in the reconstructed interferograms.

The normal vector N for the analysed three-dimensional structure is obtained as a normalised vector product of the rows of Eq. (28). Other relationships used in the process of calculations coincide with the previously described ones for planar structures.

4.2 Determination of the interference bands in holographic interferograms

The distribution of intensity of the laser beam $a^2(x,y)$ is assumed (Vest (1979)):

$$a^2(x,y) = I_L \left(k_d (N \cdot L) + k_s (V \cdot R)^n \right), \tag{30}$$

where I_L is the intensity of the incident laser beam, k_d is the diffuse reflection coefficient, k_s – the specular reflection coefficient, n is a coefficient describing the smoothness of the surface, V is the direction to the viewer, dot in parenthesis denotes a scalar product.

When the surface of the plate performs harmonic oscillations according to an appropriate eigenform, the intensity can be calculated on the basis of Eq. (4):

$$I = \left(\overline{\cos\left(4\pi (u \cdot L) \sin \omega t / \lambda\right)} \right)^2 a^2(x,y), \tag{31}$$

where u is the amplitude of harmonic oscillations, λ is the laser wavelength, the top line denotes averaging by time.

The first term of Eq. (31) corresponds to the direct calculation of the real part of Eq. (5); the imaginary part is infinitesimal:

$$\lim_{T \to \infty} \frac{1}{T} \int_0^T \sin\left(\frac{4\pi}{\lambda} (u \cdot L) \sin \omega t \right) dt = 0. \tag{32}$$

Numerical averaging of Eq. (31) can be performed using a certain number of intermediate state positions of the surface during one cycle of oscillations. The averaged term takes the form:

$$\overline{\cos\left(4\pi (u \cdot L) \sin \omega t / \lambda\right)} = \frac{1}{n} \sum_{i=1}^n \cos\left(\frac{4\pi}{\lambda} (u \cdot L) \sin \frac{2\pi (i-1)}{n} \right). \tag{33}$$

It can be noted that such averaging procedure enables to generalise the calculation of intensity for more complex (not only harmonic) dynamic processes. The convergence of the square of Eq. (33) to the square of Eq. (6) can be analysed numerically. It can be noted that when $n = 16$ the precision of calculations is acceptable for the first three interference bands, when $n = 32$ – for the first five bands, when $n = 64$ – for the first 8 bands.

The intensity levels decrease rapidly with the number of the intereference band due to the qualities of Bessel functions. As a limited number of intensity levels is used for the digital

representation of images for better visualisation of the results of calculations a sigmoidal mapping function is used to distort the intensity scale:

$$F(I) = \frac{\tanh(kI)}{\tanh(k)}, \tag{34}$$

where parameter k characterises the level of distortion, $0 < k < \infty$ (Fig. 12). It can be noted, that

$$\begin{aligned} &F(0) = 0, \\ &F(1) = 1, \\ &\lim_{k\to\infty} F(I) = \text{sign}(I), \\ &\lim_{k\to 0} F(I) = I. \end{aligned} \tag{35}$$
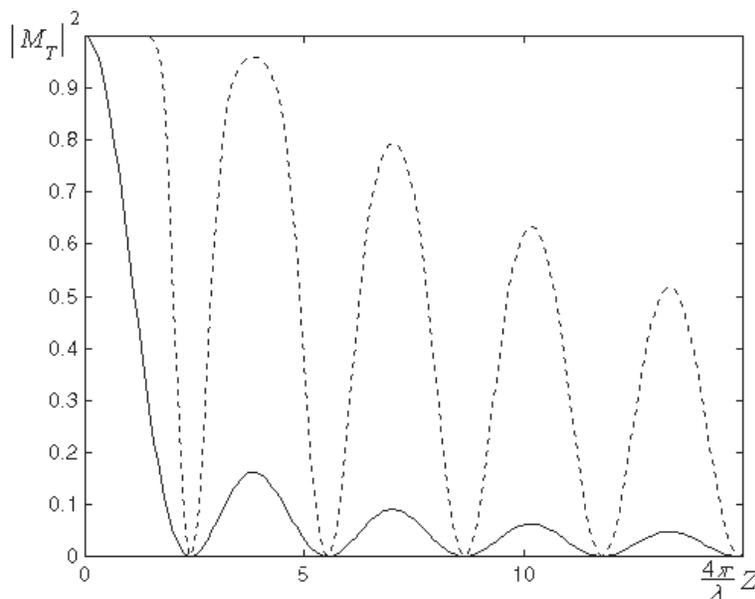

Fig. 12. The decay of intensity for the time averaged method without (solid line) and with intensity mapping at $k = 5$ (dashed line)

In fact,

$$\lim_{k\to 0} \frac{dF(I)}{dI} = \lim_{k\to 0} \frac{e^k + e^{-k}}{e^k - e^{-k}} \frac{d}{dI}\left(\frac{e^{kI} - e^{-kI}}{e^{kI} + e^{-kI}}\right) = \lim_{k\to 0} \frac{2k}{e^k - e^{-k}} = 1. \tag{36}$$

Optical stroboscopic method is used for better interpretation of micro vibrations (Vest (1979)). The structure is lightened two times per period of oscillations at the moments of extreme deflections.

The term $\overline{\cos(4\pi(u\cdot L)\sin\omega t/\lambda)}$ is interpreted as the average value of the two extreme deflections of the structure, corresponding to the moments $\omega t = \pi/2$ and $\omega t = 3\pi/2$, so the averaged term takes the form $\cos(4\pi(u\cdot L)/\lambda)$ due to the evenness of the cosine function. The Eq. (31) is transformed to:

$$I = \cos^2\left(4\pi\left(u \cdot L\right)/\lambda\right) I_L \left(k_d\left(N \cdot L\right) + k_s\left(V \cdot R\right)^n\right). \tag{37}$$

The decay of intensities for the time averaged and stroboscopic models are presented in Fig. 13. It can be noted that the locations of the centers of dark interference bands for the stroboscopic method (dashed line) do not coincide with the time averaged ones (solid line).
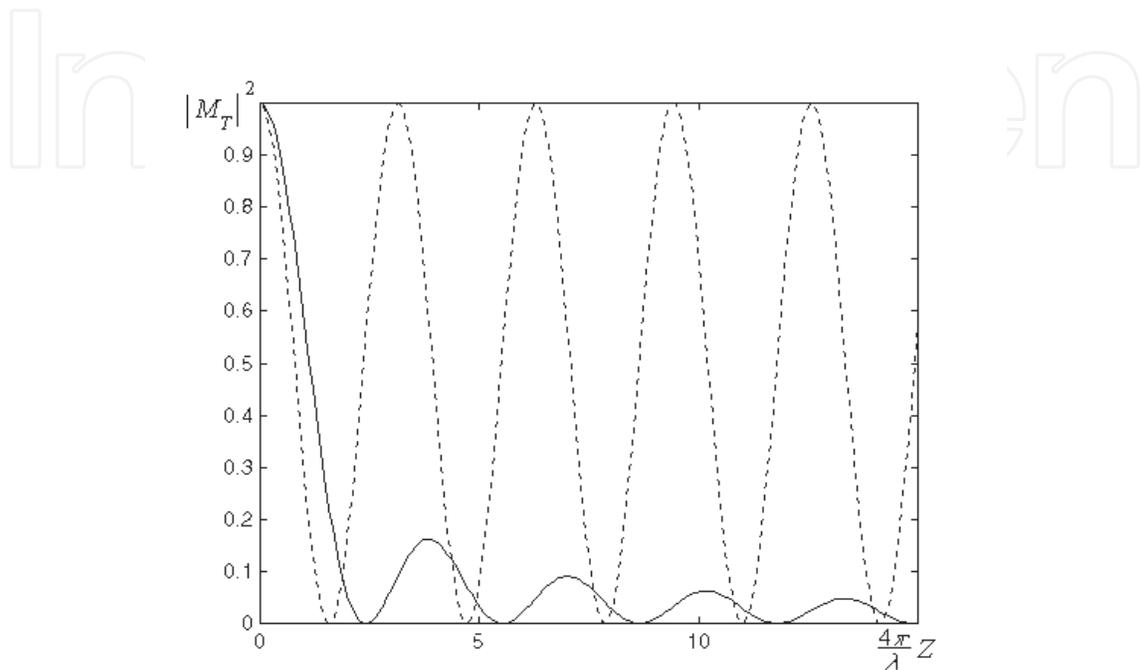

Fig. 13. The decay of intensity for the time averaged method (solid line) and for the stroboscopic method (dashed line)

The stroboscopic method does not produce a fast decay of the intensities and thus enables to interpret the higher interference bands from the interferogram. Thus the visualisation of higher amplitudes (higher interference bands) requires either the intensity mapping of the time averaged interferograms, or application of the stroboscopic method of analysis.

The problem of visualisation of microvibrations is important in engineering of precise mechanical systems. The plotting of interference bands from the results of finite element analysis has clear physical background compared to other visualisation techniques. Also that is important because of the ability of direct comparisons with the experimental results of holographic optical analysis. Presented methodology for plotting holographic interferograms is scalable in parallel computations and applicable to a wide variety of problems.

5. Computational visualization of time averaged holographic interferograms of the MEMS cantilever

The presented procedure for real time calculation of definite integrals can be effectively applied in hybrid numerical-experimental techniques where time average intensities of illumination in a holographic interferogram are reconstructed in virtual computational environment. Implementation of the proposed integration rule enables full real time computations with minimal data queue lengths and effective management of integration order.

These simulation results are illustrated for the dynamics of the MEMS cantilever under oscillating charge excitation what provides rather complex dynamic response of the tip of the cantilever. Figure 14 presents interferograms for the first eight eigenmodes. The displacement of the tip of the cantilever is presented in Fig. 15. Computations of the intensity of illumination for different time exposures for the MEMS cantilever are used to construct numerical approximations of holographic interferograms; the results are presented in Fig. 16.
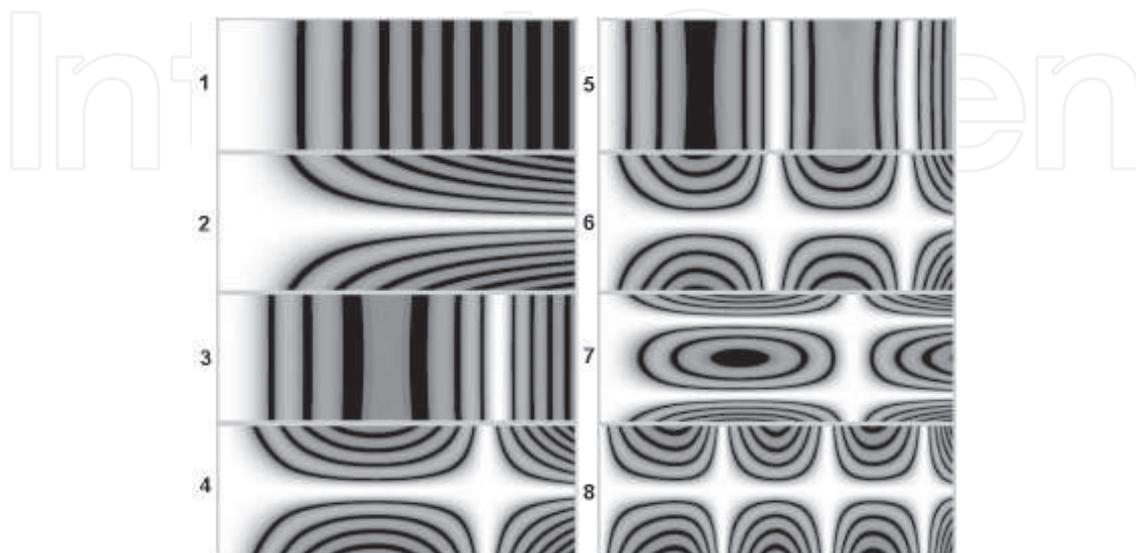
Fig. 14. Time average interferograms of the first eight eigenmodes of MEMS cantilever
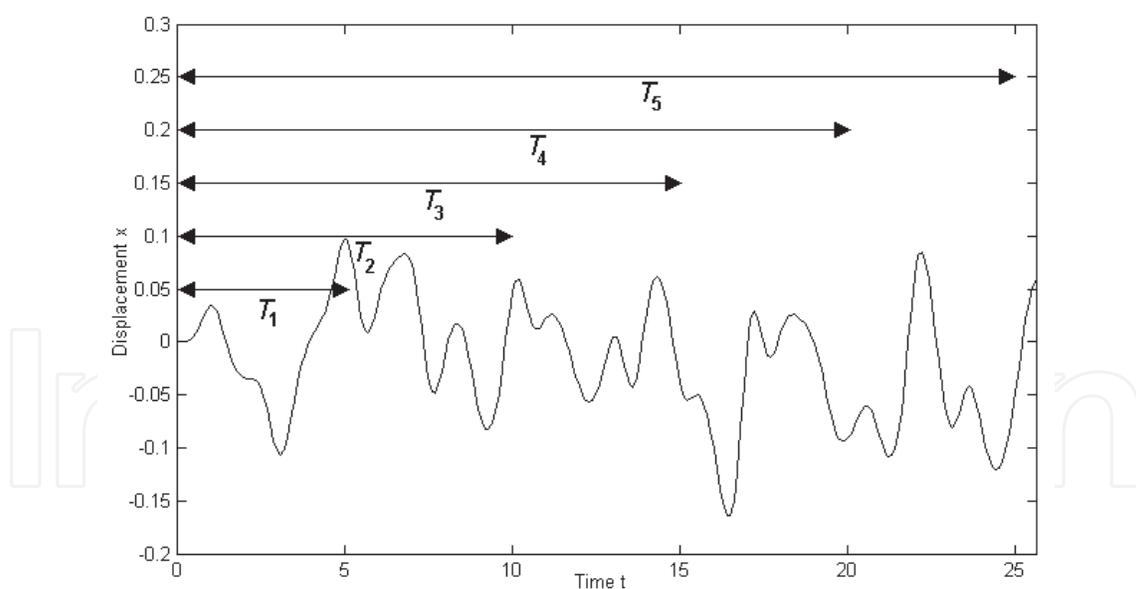
Fig. 15. Chaotic dynamics of the tip of MEMS cantilever and times of exposure $T_1 - T_5$

Numerical results validate the theoretical predictions and help to explain the complexity of the dynamical processes taking place in the analysed MEMS systems, especially when the analysed system oscillates chaotically.

Though time average holography is a powerful experimental technique for analysis of MEMS dynamics, the interpretation of produced patterns of fringes in holograms must be performed with care. Complex physical and non-linear dynamical processes taking place in MEMS
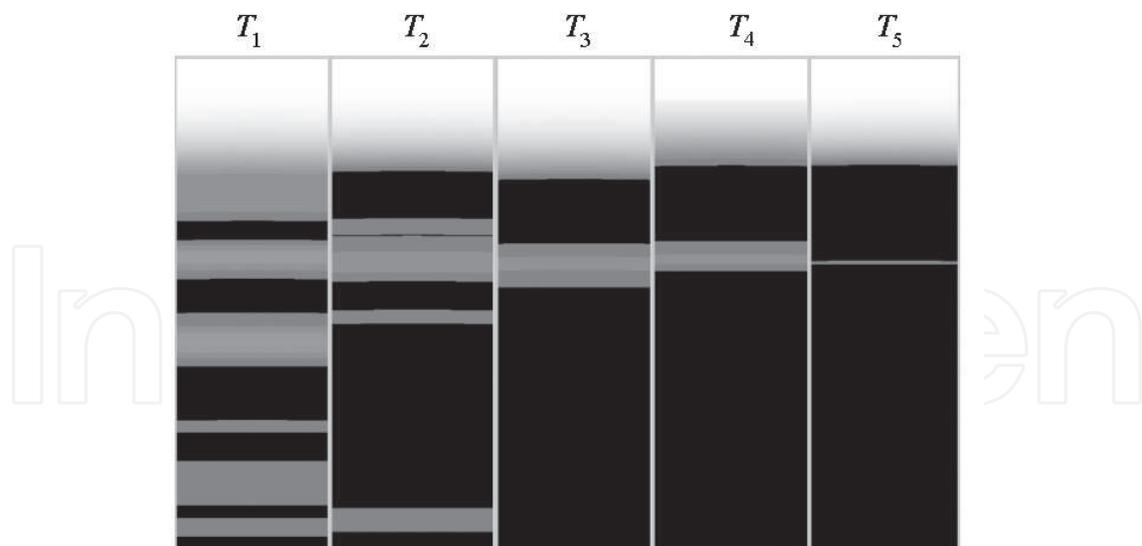
Fig. 16. Time avegare interferograms of the MEMS cantilever at different times of exposure

systems may influence the results produced by optical methods. This book chapter provides insight in the complexity of the MEMS dynamics and the problems of its optical analysis based on holographic interferometry.

6. Concluding remarks

The validation of experimental investigations versus numerical analysis provides the necessary background to analyse the dynamical characteristics of MEMS elements in virtual numerical environments. Direct application of fringe counting techniques for reconstruction of motion from time average holograms cannot be straightforward if the analysed MEMS system performs chaotic oscillations. Modifications of a classical time average holographic technique enable qualitative analysis of MEMS and can be applied for investigation of dynamical properties of much broader classes of MEMS systems.

Is well known that non-linear systems can exhibit periodic, quasiperiodic, and even chaotic responses under periodic forcing. Therefore it is important to understand what time averaged image would be produced if time average holographic interferometry is used to explore a chaotically oscillating elastic structure.

The ability to interpret such holographic interferograms would help to improve the uncertainty of the inverse problem and to distinguish malfunctions of the optical setup and also physical reasons causing specific optical effects.

7. Appendix A

Denoting shape functions L_1, L_2 and L_3 as L-coordinates of the triangle (Zienkiewicz & Morgan (2006)), and L_4 and L_5 as L-coordinates of the line, the following relationships are true:

$$\begin{aligned}
x &= L_1 x_1 + L_2 x_2 + L_3 x_3, \\
y &= L_1 y_1 + L_2 y_2 + L_3 y_3, \\
z &= L_1 z_1 + L_2 z_2 + L_3 z_3, \\
L_1 &+ L_2 + L_3 = 1,
\end{aligned} \tag{38}$$

and

$$
\begin{aligned}
x &= L_4 \tilde{x}_1 + L_5 \tilde{x}_2, \\
y &= L_4 \tilde{y}_1 + L_5 \tilde{y}_2, \\
z &= L_4 \tilde{z}_1 + L_5 \tilde{z}_2, \\
L_4 &+ L_5 = 1,
\end{aligned}
\tag{39}
$$

where $x_i, y_i, z_i, i = 1, 2, 3$ – coordinates of three points in a plane, $\tilde{x}_1, \tilde{x}_2, \tilde{x}_3$ and $\tilde{y}_1, \tilde{y}_2, \tilde{y}_3$ – coordinates of two points lying on the line. Then the L-coordinates of the point of intersection between the line and the plane are given by the solution of the following system of equations:

$$
\begin{bmatrix}
x_1 & x_2 & x_3 & -\tilde{x}_1 & -\tilde{x}_2 \\
y_1 & y_2 & y_3 & -\tilde{y}_1 & -\tilde{y}_2 \\
z_1 & z_2 & z_3 & -\tilde{z}_1 & -\tilde{z}_2 \\
1 & 1 & 1 & 0 & 0 \\
0 & 0 & 0 & 1 & 1
\end{bmatrix}
\begin{Bmatrix}
L_1 \\ L_2 \\ L_3 \\ L_4 \\ L_5
\end{Bmatrix}
=
\begin{Bmatrix}
0 \\ 0 \\ 0 \\ 1 \\ 1
\end{Bmatrix}.
\tag{40}
$$

The line intersects the plane inside the triangle when the conditions

$$
L_i \in [0, 1], \quad i = 1, 2, 3
\tag{41}
$$

are satisfied.

8. References

Caponero, M.A.; Pasqua, P.; Paolozzi, A. & Peroni, I. (2000). Use of holographic interferometry and electronic speckle pattern interferometry for measurements of dynamic displacements, *Mechanical Systems and Signal Processing*, Vol.14, No.1, 49–62, ISSN 0888-3270.

Davis, P.J. & Rabinowitz, P. (1984). *Methods of Numerical Integration*, Academic Press, ISBN 978-0122063602, New York.

Fagan, W.F., Waddell, P. & McCracken, W. (1972). The study of vibration patterns using real-time hologram interferometry, *Optics & Laser Technology*, Vol.4, No.4, 167–172, ISSN 0030-3992.

Fein, H. (2000). Holographic interferometry: nondestructive tool, *The industrial Physicist*, Vol.3, No.3, 37–39, ISSN 1082-1848.

Ganesan, A.R.; Hinsch, K.D. & Meinlschmidt P. (2000). Transition between rationally and irrationally related vibration modes in time-average holography, *Optics Communications*, Vol.174, No.5-6, 347–353, ISSN 0030-4018.

Ivanov, V.P. & Batrakov, A.S. (1995). *Three Dimensional Computer Graphics*, Radio i Sviaz, Moscow.

Mattson, T.; Sanders, B. & Massingill, B. (2004). *Patterns for Parallel Programming*, Addison Wesley Professional, ISBN 0-321-22811-1, Reading, Massachusetts.

Ostasevicius, V.; Palevicius, A.; Daugela, A; Ragulskis, M. & Palevicius, R. (2004). Holographic imaging technique for characterization of MEMS switch dynamics, *SPIE Proceedings, 2004*, 73–84, ISSN 0277-786X.

Ostasevicius, V.; Tamulevicius, S.; Palevicius, A.; Ragulskis, M; Grigaliunas, V. & Minialga, V. (2005). Synergy of contact and non-contact techniques for design and characterization of vibrating MOEMS elements, *Journal of Microlithography, Microfabrication, and Microsystems*, Vol. 4, No. 4, 1–9, ISSN 1537-1646.

Ragulskis, M.; Palevicius, A. & Ragulskis, L. (2003). Plotting holographic interferograms for visualisation of dynamic results from finite element calculations, *International Journal for Numerical Methods in Engineering*, Vol. 56, 1647-1659, ISSN 0029-5981.

Ragulskis, M. & Saunoriene, L. (2007). Order adaptive quadrature rule for real time holography applications, *Lecture Notes in Computer Science*, Vol. 4310, 685–692, ISSN 0302-9743.

Ragulskis, M. & Saunoriene, L. (2008). Generalisations of the compound trapezoidal rule, *Applied Numerical Mathematics*, Vol.58 , No.1, 40–58, ISSN 0168-9274.

Rastogi, P.K. (2000). Principles of holographic interferometry and speckle metrology, *Photomechanics Topics in Applied Physics*, Vol. 77, 103–150, ISSN 0303-4216.

Vest, C.M. (1979). *Holographic Interferometry*, Wiley, ISBN 978-0471906834, New York.

Zienkiewicz, O.C. & Morgan, K. (2006). *Finite Elements and Approximation*, Dover Publications, ISBN 0486453014, New York.
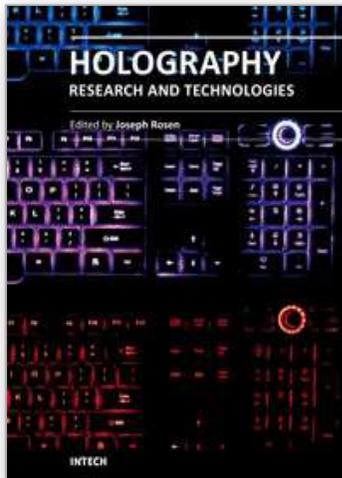
Holography has recently become a field of much interest because of the many new applications implemented by various holographic techniques. This book is a collection of 22 excellent chapters written by various experts, and it covers various aspects of holography. The chapters of the book are organized in six sections, starting with theory, continuing with materials, techniques, applications as well as digital algorithms, and finally ending with non-optical holograms. The book contains recent outputs from researches belonging to different research groups worldwide, providing a rich diversity of approaches to the topic of holography.

How to reference

In order to correctly reference this scholarly work, feel free to copy and paste the following:

Minvydas Ragulskis, Arvydas Palevicius and Loreta Saunoriene (2011). Hybrid Numerical-Experimental Holographic Interferometry for Investigation of Nonlinearities in MEMS Dynamics, Holography, Research and Technologies, Prof. Joseph Rosen (Ed.), ISBN: 978-953-307-227-2, InTech, Available from: http://www.intechopen.com/books/holography-research-and-technologies/hybrid-numerical-experimental-holographic-interferometry-for-investigation-of-nonlinearities-in-mems

INTECH
open science | open minds